

# One-Dimensional Maxwell-Schrödinger Hybrid Simulation of Transmon Qubits

Thomas E. Roth *Member, IEEE*, and Samuel T. Elkin *Member, IEEE*

**Abstract**—Transmon quantum bits (qubits) are one of the most popular experimental platforms currently being pursued for developing quantum information processing technologies. In these devices, applied microwave pulses are used to control and measure the state of the transmon qubit. Currently, the design of the microwave pulses for these purposes is done through simple theoretical and/or numerical models that neglect how the transmon can modify the applied microwave field. In this work, we present the formulation and finite element time domain discretization of a semiclassical Maxwell-Schrödinger hybrid method for describing the dynamics of a transmon qubit capacitively coupled to a transmission line system. Numerical results are presented using this Maxwell-Schrödinger method to characterize the control and measurement of the state of a transmon qubit. We show that our method matches standard theoretical predictions in relevant operating regimes, and also show that our method produces physically meaningful results in situations where the theoretical models break down. In the future, our method can be used to explore broader operating regimes to search for more effective control and measurement protocols for transmon qubits.

**Index Terms**—Hybrid modeling, computational electromagnetics, circuit quantum electrodynamics, transmon qubit.

## I. INTRODUCTION

**S**UPERCONDUCTING circuit architectures are one of the leading approaches for developing quantum information processing technologies [1]–[3]. These hardware platforms are very flexible, and have been used to implement a myriad range of technologies including analog and digital quantum computers [4]–[8], single photon sources [9]–[11], quantum memories [12], [13], and other components of quantum communication systems [14], to name a few. In all of these technologies, a combination of classical and quantum microwave fields are used to interact with large coherent collections of charges in superconducting circuits, leading to these systems being referred to as circuit quantum electrodynamics (cQED) devices. Recent achievements of a computational “quantum advantage” has demonstrated the great progress made with these hardware platforms [6], [7], but has also highlighted that many significant engineering challenges remain for these technologies to reach their full potential.

Manuscript received XXXX XX, 2022; revised XXXX XX, 2022.

This work was funded by a startup fund at Purdue University. (*Corresponding author: Thomas E. Roth.*)

Thomas E. Roth is with the Elmore Family School of Electrical and Computer Engineering, Purdue University, West Lafayette, IN 47907 USA (e-mail: rothte@purdue.edu).

Samuel T. Elkin was with the Elmore Family School of Electrical and Computer Engineering, Purdue University, West Lafayette, IN 47907 USA. He is now with Indesign, LLC., Indianapolis, IN 46216 USA.

This work has been submitted to the IEEE for possible publication. Copyright may be transferred without notice, after which this version may no longer be accessible.

Some of the most pressing challenges involve the need to significantly increase the number of quantum bits (qubits) in the devices, while further improving the qubit coherence and the speed and fidelity of qubit control and measurement [8], [15]. This is necessitating the exploration of new packaging and integration strategies [16]–[18], as well as miniaturization of control and measurement electronics [19]–[21]. To explore the design space of these emerging device approaches, higher-fidelity numerical modeling methods are becoming increasingly necessary [22]–[26]. However, these modeling methods are still in their infancy, with existing methods often requiring tedious and computationally costly approaches to perform an eigenmode decomposition of the electromagnetic system the qubits are coupled to [22]–[24]. These methods will significantly struggle to scale to systems with many qubits, and so it is of interest to develop efficient high-fidelity numerical modeling methods for cQED devices.

One avenue to satisfy these modeling needs is with self-consistent semiclassical models that treat certain electromagnetic effects classically and the qubit dynamics quantum mechanically [27]. Semiclassical modeling has a long history in studying large-scale atom-field interactions like those involved in lasers [28], but have more recently begun being used in optical frequency regimes to analyze how classical electromagnetic fields interact with the states of individual quantum systems [29]–[33]. Often referred to as Maxwell-Schrödinger hybrid methods, these approaches have thus far been overlooked for cQED systems, despite the more prominent role that classical microwave fields play in both the control and measurement of qubit states in comparison to optical frequency technologies [1]–[3].

In this work, we present the first systematic formulation of semiclassical equations of motion for a transmon qubit coupled to a microwave transmission line network. We focus specifically on transmon qubits to make the discussion concrete, and because this is the leading superconducting circuit qubit used experimentally in current devices [34], [35]. In addition to formulating the semiclassical equations of motion, we also propose a suitable one-dimensional Maxwell-Schrödinger hybrid method to discretize the system of equations. We validate our approach by comparing our numerical results to established theoretical predictions for the control and measurement of the state of a transmon qubit. Our semiclassical framework provides new insights into how classical microwave fields interact with transmon qubits, and also provides a scalable method that can be generalized in a straightforward manner to situations where purely theoretical treatments of these coupled systems become prohibitively cumbersome.

The remainder of this work is organized in the following

manner. In Section II, we present the derivation of a self-consistent set of semiclassical equations of motion that characterize the interactions between classical microwave signals and a transmon qubit. We then describe a suitable one-dimensional Maxwell-Schrödinger hybrid method to numerically solve the semiclassical equations of motion in Section III. Our approach is specifically designed to ease the transition to a full-wave three-dimensional Maxwell-Schrödinger method in the future. We present a range of numerical results in Section IV to validate our numerical method against established theoretical predictions. Finally, we discuss conclusions and directions for future work in Section V.

## II. FORMULATION

In this section, we present the derivation of a set of self-consistent semiclassical equations of motion for a transmon qubit capacitively coupled to a microwave transmission line. To guide the derivation, we follow a Hamiltonian mechanics approach that represents a natural approach for incorporating the quantum effects of the transmon qubit (for an introduction to Hamiltonian mechanics in the context of electromagnetics, we refer readers to [36]–[38]). Given that a Hamiltonian mechanics analysis of a transmission line is not commonly encountered, we begin in Section II-A by demonstrating the basic process for an isolated transmission line to introduce the general concepts and physical quantities that will be used throughout this work. Following this, we show in Section II-B how a similar Hamiltonian analysis approach can be used to arrive at a “phase space” Schrödinger equation to describe the transmon qubit. Finally, we present the derivation of the equations of motion for the coupled system in Section II-C.

### A. Hamiltonian Mechanics of a Transmission Line

Formulating the Hamiltonian of an isolated transmission line is fairly straightforward in terms of voltages and currents on the transmission line. The Hamiltonian corresponds to the total energy on the transmission line, which from basic transmission line theory can be readily identified as

$$H_{\text{TR}} = \frac{1}{2} \int [C(V(z,t))^2 + L(I(z,t))^2] dz, \quad (1)$$

where  $V$  is the voltage,  $I$  is the current, and  $L$  and  $C$  are the per-unit-length inductance and capacitance, respectively. Although this is easy to formulate, voltage and current are not appropriate conjugate variables for a Hamiltonian mechanics analysis, much like how electric and magnetic fields are not suitable conjugate variables [36]. Correspondingly, we must use transmission line parameters that are more “like” the electromagnetic potentials (which are suitable conjugate variables).

The particular convention that is most useful here is to describe the transmission line in terms of nodal flux  $\phi$  and nodal charge  $Q$  [39], [40]. Physically, we have that the nodal flux is given by

$$\phi(z,t) = \int_{-\infty}^t V(z,\tau) d\tau. \quad (2)$$

The nodal flux may also be related to the current on the transmission line as

$$I(z,t) = -L^{-1} \partial_z \phi(z,t). \quad (3)$$

The nodal charge  $Q$  is the variable that is canonically conjugate to  $\phi$ . For an isolated transmission line, we have that

$$Q(z,t) = C \partial_t \phi(z,t). \quad (4)$$

From this and (2), it is tempting to relate the nodal charge directly to the voltage as  $Q = CV$ , which has a form that is intuitive from the definition of capacitance. Although this is the case for this simple example, it is important to stress that physically the voltage is defined through (2) in our Hamiltonian formalism, and so we will not always find the direct relationship of  $Q = CV$ . This is a consequence of choosing  $Q$  as the canonical conjugate variable in the Hamiltonian formalism, which forces it to take on whatever characteristics are needed such that  $\phi$  and  $Q$  vary in time in tandem to conserve energy [36].

Now, in terms of  $\phi$  and  $Q$ , we can rewrite the Hamiltonian (1) as

$$H_{\text{TR}} = \frac{1}{2} \int [C^{-1}(Q(z,t))^2 + L^{-1}(\partial_z \phi(z,t))^2] dz. \quad (5)$$

We can now use Hamilton’s equations to derive the equations of motion for  $\phi$  and  $Q$  [36]. We will then show that these can also be found from the well-known telegrapher’s equations [41] to show that this derivation approach is consistent with established transmission line theory. For  $\phi$  and  $Q$ , Hamilton’s equations are

$$\partial_t \phi = \frac{\delta H_{\text{TR}}}{\delta Q}, \quad \partial_t Q = -\frac{\delta H_{\text{TR}}}{\delta \phi}. \quad (6)$$

Assuming we have boundary conditions that cause the boundary terms that arise from integration by parts to vanish, the requisite functional derivatives can be easily evaluated to find

$$\partial_t \phi = C^{-1} Q, \quad (7)$$

$$\partial_t Q = L^{-1} \partial_z^2 \phi. \quad (8)$$

We can combine (7) and (8) to get

$$\partial_z^2 \phi - LC \partial_t^2 \phi = 0, \quad (9)$$

which we can readily recognize as a wave equation with propagation speed  $v = 1/\sqrt{LC}$ .

To see that (9) is consistent with the telegrapher’s equations, we begin by recalling that the telegrapher’s equations are

$$\partial_z V = -L \partial_t I, \quad (10)$$

$$\partial_z I = -C \partial_t V. \quad (11)$$

Starting with (11) that comes from Kirchoff’s current law [41], we can use (2) and (3) to rewrite this as

$$-L^{-1} \partial_z^2 \phi = -C \partial_t^2 \phi. \quad (12)$$

This can be easily rearranged to be seen to be equivalent with (9), as expected. We can also substitute (2) and (3) in (10) to

find that Kirchoff's voltage law becomes

$$\partial_z \partial_t \phi = \partial_t \partial_z \phi, \quad (13)$$

which will always hold for practical cases of interest. Hence, so long as we solve the wave equation given in (9), we find that our results will be consistent with traditional transmission line theory.

### B. Hamiltonian Mechanics of a Transmon Qubit

Traditionally, the Hamiltonian operator for a transmon qubit is given as

$$\hat{H} = 4E_C(\hat{n} - n_g)^2 - E_J \cos \hat{\varphi}, \quad (14)$$

where  $\hat{n}$  is the charge operator of the qubit and  $\hat{\varphi}$  is the Josephson phase operator of the qubit [34], [35]. The classical real-valued quantity  $n_g$  is the offset charge that can be used to describe how voltages modify the equilibrium value of charges in the qubit. Finally,  $E_C$  and  $E_J$  are the charging and Josephson energies of the qubit, respectively. Explicitly, we have that  $E_C = e^2/2C_\Sigma$ , where  $e$  is the electron charge and  $C_\Sigma$  is the total capacitance to ground from the terminals of the Josephson junction in the transmon qubit [34], [35]. The Josephson energy is related to design parameters of the Josephson junction in the qubit, which will not need to be considered explicitly in this work.

Note that the transmon qubit is specifically designed to be less sensitive to  $n_g$  in the asymptotic regime of  $E_J/E_C \gg 1$ , since common sources of noise can be effectively considered as corresponding to a fluctuating  $n_g$  value [34], [35]. Due to the reduced sensitivity to  $n_g$ , this parameter is often neglected in the analysis of transmon qubits. However, for practical ratios of  $E_J/E_C$ , higher energy levels of the transmon qubit are still impacted by the value of  $n_g$ . Hence, we retain this parameter in our model so that the influence of these higher energy levels can be accounted for within the numerical method, although exhaustively exploring the effects of  $n_g$  on the system dynamics are outside of the scope of this work.

Now, working directly with (14) is not suitable for developing our desired semiclassical equations of motion. Instead, it is more convenient to consider the transmon Hamiltonian operator in the phase basis of  $\hat{\varphi}$  so that the Hamiltonian operator becomes a differential operator that can be incorporated into the form of Schrödinger's equation [34]. In this new representation, we have that the phase operator  $\hat{\varphi}$  becomes a regular position variable  $\varphi$  and the charge operator  $\hat{n}$  becomes  $-i\partial_\varphi$  [42]. We then have that the time-dependent Schrödinger equation using the Hamiltonian operator of (14) can be written as

$$[4E_C(-i\partial_\varphi - n_g)^2 - E_J \cos \varphi] \psi(\varphi, t) = i\hbar \partial_t \psi(\varphi, t), \quad (15)$$

where  $\psi$  is a complex-valued wavefunction with a standard probabilistic interpretation that also satisfies periodic boundary conditions of  $\psi(\varphi, t) = \psi(\varphi + 2\pi, t)$  [34].

In order to follow a Hamiltonian mechanics derivation of the coupled semiclassical equations of motion, we need to determine a Hamiltonian that will give us (15) through Hamilton's equations. This process is often done in quantum

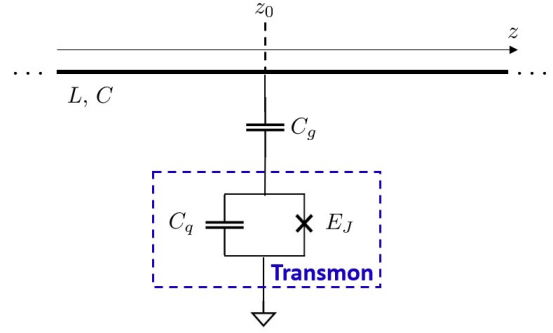


Fig. 1: Schematic of a transmon qubit capacitively coupled to a transmission line with per-unit-length parameters of  $L$  and  $C$ . A transmon qubit is composed of a capacitance  $C_q$  in parallel with a Josephson junction that has Josephson energy  $E_J$ .

field theory where it is useful to perform a second quantization of a Schrödinger wave field [43], [44]. We will follow this example, but will not perform a second quantization of the system, favoring the interpretation of  $\psi$  given above.

Considering this, we propose a Schrödinger wave field Hamiltonian of

$$H_T = \int_{-\pi}^{\pi} \frac{1}{i\hbar} \Pi(\varphi, t) \left[ 4E_C(-i\partial_\varphi - n_g)^2 - E_J \cos \varphi \right] \psi(\varphi, t) d\varphi. \quad (16)$$

In (16), we have that  $\Pi = i\hbar\psi^*$  is the conjugate function to  $\psi$  [43], [44]. We then have that Hamilton's equations for  $\psi$  and  $\Pi$  are

$$\partial_t \psi = \frac{\delta H_T}{\delta \Pi}, \quad \partial_t \Pi = \frac{\delta H_T}{\delta \psi}. \quad (17)$$

Evaluating the first functional derivative, we readily find that

$$\partial_t \psi(\varphi, t) = \frac{1}{i\hbar} [4E_C(-i\partial_\varphi - n_g)^2 - E_J \cos \varphi] \psi(\varphi, t), \quad (18)$$

which is equivalent to (15), as desired. One can also find the equation of motion for  $\Pi$ , but this is easily found to be equivalent to the complex conjugate of (18). Although this is important for a second quantization procedure, it is not necessary for our current purposes.

### C. Self-Consistent Semiclassical Equations of Motion

We can now formulate the total Hamiltonian for a transmon qubit capacitively coupled to a transmission line, as shown in Fig. 1, by generalizing the results of [23], [34]. In particular, the total Hamiltonian is given by

$$H = H_{TR} + H_T + H_I, \quad (19)$$

where  $H_{TR}$  is given in (5),  $H_T$  is given in (16), and  $H_I$  is the interaction Hamiltonian characterizing the coupling between the subsystems. For this kind of capacitive coupling, the interaction Hamiltonian is often expressed as [34]

$$H_I = 2e\beta C^{-1} Q(z_0, t) \hat{n}, \quad (20)$$

where  $\beta = C_g/C_\Sigma$ ,  $C_\Sigma = C_g + C_q$  (the definitions of these capacitances can be found in Fig. 1), and  $z_0$  is the location on

the transmission line that the transmon is capacitively coupled to. Translating this into a format that is compatible with our expressions for  $H_{\text{TR}}$  and  $H_{\text{T}}$ , we have that

$$H_{\text{I}} = \int \int_{-\pi}^{\pi} \frac{2e\beta}{i\hbar C} Q(z, t) \delta(z - z_0) \times \Pi(\varphi, t) (-i\partial_{\varphi} \psi(\varphi, t)) d\varphi dz. \quad (21)$$

The coupled equations of motion for this system can now be found using appropriate versions of Hamilton's equations. For the transmission line variables, we have that

$$\partial_t \phi = \frac{\delta H}{\delta Q}, \quad \partial_t Q = -\frac{\delta H}{\delta \phi}. \quad (22)$$

Using these, we find that

$$\partial_t \phi = C^{-1} Q + C^{-1} \delta(z - z_0) 2e\beta \langle n(t) \rangle, \quad (23)$$

where

$$\langle n(t) \rangle = \int_{-\pi}^{\pi} \psi^*(\varphi, t) (-i\partial_{\varphi} \psi(\varphi, t)) d\varphi \quad (24)$$

is the expectation value of the charge operator  $\hat{n}$ . Similarly, for  $Q$  we have

$$\partial_t Q = L^{-1} \partial_z^2 \phi. \quad (25)$$

Combining (23) and (25), we get a wave equation for  $\phi$  of

$$\partial_z^2 \phi - LC \partial_t^2 \phi = -\delta(z - z_0) L 2e\beta \partial_t \langle n(t) \rangle. \quad (26)$$

Physically, the right-hand side of (26) can be interpreted as a semiclassical current source due to changes in the expectation value of charge in the transmon. This current source is similar to the transmon current density discussed in [23], and also matches the expectation that the coupling from the quantum system into the classical one in a semiclassical treatment should involve an expectation value of a current operator [27].

Next, we can find the equation of motion for  $\psi$  from

$$\partial_t \psi = \frac{\delta H}{\delta \Pi}. \quad (27)$$

Evaluating the functional derivative gives the time-dependent Schrödinger equation

$$[4E_C (-i\partial_{\varphi} - n_g)^2 - E_J \cos \varphi - i2e\beta C^{-1} Q(z_0, t) \partial_{\varphi}] \psi(\varphi, t) = i\hbar \partial_t \psi(\varphi, t). \quad (28)$$

As mentioned previously, we can find a similar equation for  $\Pi$ , but we will not need to use it here so we omit those details.

Moving forward, it is necessary to rewrite the term involving  $Q$  in (28) because we will not have access to this quantity when solving (26). To address this, we rearrange (23) at  $z = z_0$  to find

$$Q(z_0, t) = C \partial_t \phi(z_0, t) - 2e\beta \langle n(t) \rangle. \quad (29)$$

Substituting this into (28) for  $Q$ , we get

$$[4E_C (-i\partial_{\varphi} - n_g)^2 - E_J \cos \varphi] \psi(\varphi, t) - i[2e\beta \partial_t \phi(z_0, t) - (2e\beta)^2 C^{-1} \langle n(t) \rangle] \partial_{\varphi} \psi(\varphi, t) = i\hbar \partial_t \psi(\varphi, t). \quad (30)$$

The term involving  $\langle n(t) \rangle$  leads to a nonlinearity in the

Schrödinger equation that is inconvenient to deal with numerically. However, for the operating characteristics of most systems, this nonlinear correction is typically significantly smaller than the  $\partial_t \phi$  term so that we choose to neglect it here.

More explicitly, for most devices the per-unit-length capacitance of the transmission line will be  $O(100 \text{ pF/m})$  and the coupling strength  $\beta$  will typically be  $\sim 0.1$  or significantly smaller depending on the purpose of the transmission line (e.g., for controlling the state of the qubit versus measuring the state). The voltage on the transmission line (given by  $\partial_t \phi(z_0, t)$ ) will typically be in the nanovolt to microvolt range, while  $\langle n(t) \rangle$  will realistically have a maximum of  $O(1)$ . As a result, the term involving  $\langle n(t) \rangle$  will often be a few orders of magnitude smaller than the term involving  $\partial_t \phi$ , allowing it to be neglected. It should be emphasized that this approximation only neglects how the instantaneous correction of the voltage on the transmission line due to changes in the charge state of the transmon affects the charge state of the transmon. The overall equations of motion still incorporate the effect of the charge state of the transmon on the voltage in the transmission line through the semiclassical current source, which then get fed back to the transmon after advancing the equations of motion in time in a leapfrog time marching approach.

Considering this, we drop the  $\langle n(t) \rangle$  term in (30) to get

$$[4E_C (-i\partial_{\varphi} - n_g)^2 - E_J \cos \varphi] \psi(\varphi, t) - i2e\beta (\partial_t \phi(z_0, t)) \partial_{\varphi} \psi(\varphi, t) = i\hbar \partial_t \psi(\varphi, t). \quad (31)$$

This equation can be solved in tandem with (26) to describe the semiclassical interactions between the transmon qubit and a transmission line.

### III. DISCRETIZATION

In this section, we discuss the development of a suitable Maxwell-Schrödinger numerical method to solve (26) and (31) together. In particular, we utilize a first-order finite element time domain (FETD) method to discretize both sets of equations, which we then solve in tandem using a leapfrog time marching strategy. Given the one-dimensional spatial nature of the two equations, a finite element discretization is unnecessarily complicated to achieve a desired level of numerical accuracy. We follow this approach here so that our resulting matrix system has a similar structure to what would be encountered when adapting this method to a three-dimensional full-wave Maxwell-Schrödinger method in the future, where the advantages of a FETD method over other simpler discretization strategies are more clear.

The remainder of this section is organized in the following manner. In Section III-A, we describe the discretization and time marching procedure when a standard first-order FETD approach is used for solving (26) and (31) together. Following this, we discuss in Section III-B a strategy for improving the efficiency of the method by discretizing the time-dependent Schrödinger equation (31) in terms of eigenstates of the free transmon Hamiltonian operator (14). This approach is also of particular interest for extending these methods to handling multiple qubits simultaneously, which will be considered in

future work. Finally, we present a stability analysis in Section III-C of the time marching approaches for the two discretization strategies discussed.

#### A. Finite Element Time Domain Discretization

To begin, we will consider the FETD discretization of (26). This follows a relatively standard FETD process (e.g., see [45]), however, the boundary conditions that need to be applied to  $\phi$  require more discussion. First, we will consider the case of a terminating resistance  $R_L$  at the end of a transmission line. Through Ohm's law, we would generally have that  $I(z_L, t) = V(z_L, t)/R_L$ , where  $z_L$  is the  $z$ -coordinate of the resistor. Using the definitions of  $V$  and  $I$  in terms of the nodal flux given in (2) and (3), we see that Ohm's law becomes

$$\partial_z \phi(z_L, t) = -\frac{L}{R_L} \partial_t \phi(z_L, t), \quad (32)$$

which can serve as a suitable boundary condition at the end of the transmission line.

To excite the transmission line, it is common to introduce a voltage source  $V_S(t)$  in series with a source resistance  $R_S$ . This can be re-expressed through a Norton equivalent with current source  $I_S(t) = V_S(t)/R_S$  in parallel with resistance  $R_S$ . In this case, Kirchoff's current law becomes

$$\frac{V_S(t)}{R_S} = \frac{V(z_S, t)}{R_S} + I(z_S, t), \quad (33)$$

where  $z_S$  is the  $z$ -coordinate of the source. Rewriting this in terms of the nodal flux through (2) and (3), we get

$$\partial_z \phi(z_S, t) = -\frac{L}{R_S} [V_S(t) - \partial_t \phi(z_S, t)], \quad (34)$$

which can serve as the boundary condition at the beginning of the transmission line.

We can now perform the spatial discretization of (26) by representing  $\phi$  as

$$\phi(z, t) = \sum_{n=1}^{N_\phi} N_n(z) \phi_n(t), \quad (35)$$

where  $N_n$  is the standard first-order nodal basis function (i.e., a triangular function [45]) and  $\phi_n$  is the time-dependent expansion coefficient. The weak form of (26) can be easily found by testing the equation with the same spatial functions. The resulting semi-discrete equation is

$$[T] \frac{d^2}{dt^2} \{\phi\} + [R] \frac{d}{dt} \{\phi\} + [S] \{\phi\} = \{f\}, \quad (36)$$

where  $\{\phi\} = [\phi_1, \phi_2, \dots, \phi_{N_\phi}]^T$ . Further, the matrices  $[T]$ ,  $[R]$ , and  $[S]$  are

$$[T]_{mn} = \int N_m(z) N_n(z) dz, \quad (37)$$

$$[R]_{mn} = \frac{L}{R_L} N_m(z_L) N_n(z_L) + \frac{L}{R_S} N_m(z_S) N_n(z_S), \quad (38)$$

$$[S]_{mn} = \int (\partial_z N_m(z)) (\partial_z N_n(z)) dz. \quad (39)$$

Finally, we have that elements of the excitation vector are

$$\{f\}_m = \frac{L}{R_S} N_m(z_S) V_s(t) + N_m(z_0) L 2e\beta \partial_t \langle n(t) \rangle. \quad (40)$$

We will discuss the temporal discretization of (36) after discussing the spatial discretization of (31).

The spatial discretization of (31) can follow a similar pattern. To begin, we first expand all the terms out to have

$$\begin{aligned} & [-4E_C \partial_\varphi^2 + i8n_g E_C \partial_\varphi + 4E_C n_g^2 - E_J \cos \varphi] \psi(\varphi, t) \\ & - i2e\beta (\partial_t \phi(z_0, t)) \partial_\varphi \psi(\varphi, t) = i\hbar \partial_t \psi(\varphi, t). \end{aligned} \quad (41)$$

Expanding  $\psi$  as

$$\psi(\varphi, t) = \sum_{n=1}^{N_\psi} N_n(\varphi) a_n(t) \quad (42)$$

and testing (41) with the same spatial functions, the semi-discrete version of (41) becomes

$$[E] \frac{d}{dt} \{a\} = \frac{1}{i\hbar} [H_0] \{a\} - \frac{2e\beta}{\hbar} (\partial_t \phi(z_0, t)) [Q] \{a\}, \quad (43)$$

where  $\{a\} = [a_1, a_2, \dots, a_{N_\psi}]^T$  and

$$[H_0] = 4E_C [N] + i8n_g E_C [Q] + 4E_C n_g^2 [E] - E_J [V], \quad (44)$$

$$[E]_{mn} = \int_{-\pi}^{\pi} N_m(\varphi) N_n(\varphi) d\varphi, \quad (45)$$

$$[N]_{mn} = \int_{-\pi}^{\pi} (\partial_\varphi N_m(\varphi)) (\partial_\varphi N_n(\varphi)) d\varphi, \quad (46)$$

$$[Q]_{mn} = \int_{-\pi}^{\pi} N_m(\varphi) (\partial_\varphi N_n(\varphi)) d\varphi, \quad (47)$$

$$[V]_{mn} = \int_{-\pi}^{\pi} N_m(\varphi) N_n(\varphi) \cos(\varphi) d\varphi. \quad (48)$$

Now, to solve (36) and (43) together we follow a basic leapfrog time marching strategy. To achieve this, we represent  $\phi$  and  $\psi$  on staggered temporal grids that are offset by a half time step. Choosing  $\phi$  to be represented at integer time steps, we can discretize the temporal derivatives in (36) using standard central difference formulas [45]. The resulting time stepping equation is then

$$\begin{aligned} & \left( \frac{[T]}{(\Delta t)^2} + \frac{[R]}{2\Delta t} \right) \{\phi^{(j+1)}\} = \left( \frac{2[T]}{(\Delta t)^2} - [S] \right) \{\phi^{(j)}\} \\ & - \left( \frac{[T]}{(\Delta t)^2} - \frac{[R]}{2\Delta t} \right) \{\phi^{(j-1)}\} + \{f^{(j)}\}, \end{aligned} \quad (49)$$

where  $\Delta t$  is the time step and superscript  $(j)$  denotes a vector of coefficients evaluated at  $t = j\Delta t$  with  $j$  an integer. Note that in evaluating the  $\partial_t \langle n(t) \rangle$  term in (40), we use a central difference formula that uses a time step size of  $\Delta t/2$  evaluated at  $t = j\Delta t$ . Explicitly, we have that

$$\partial_t \langle n^{(j)} \rangle = \frac{\langle n^{(j+1/2)} \rangle - \langle n^{(j-1/2)} \rangle}{\Delta t}, \quad (50)$$

which samples  $\langle n(t) \rangle$  at temporal values that  $\psi$  has already been solved at.

A similar process also works for the temporal discretization of (43), but with  $\psi$  sampled on the staggered temporal grid. Using a simple central difference discretization of (43) at time step  $(j + 1/2)\Delta t$ , we get

$$[E]\{a^{(j+3/2)}\} = [E]\{a^{(j-1/2)}\} + \frac{2\Delta t}{i\hbar}[H_0]\{a^{(j+1/2)}\} - \frac{4e\beta\Delta t}{\hbar}(\partial_t\phi^{(j+1/2)}(z_0))[Q]\{a^{(j+1/2)}\}. \quad (51)$$

To evaluate  $\partial_t\phi^{(j+1/2)}(z_0)$ , we use a time step size of  $\Delta t/2$  so that it becomes

$$\partial_t\phi^{(j+1/2)}(z_0) = \frac{\phi^{(n+1)}(z_0) - \phi^{(n)}(z_0)}{\Delta t}, \quad (52)$$

which samples  $\phi(z_0, t)$  at temporal values  $\phi$  has already been solved at.

### B. Reduced Eigenstate Discretization

In most situations, it is advantageous to consider the dynamics of a transmon in terms of its eigenstates rather than using a full spatial description like that used in Section III-A. This can be easily incorporated into a Maxwell-Schrödinger discretization, and leads to a more efficient method that also produces more intuitive results.

To do this, we first must find the eigenstates and eigenenergies of the free transmon Hamiltonian operator. These can be found analytically [34], but can also be found numerically very easily using the finite element method described in Section III-A. In particular, the  $n$ th numerical eigenstate  $\{\psi_n\}$  with corresponding eigenenergy  $E_n$  can be found as solutions to the generalized eigenvalue problem

$$[H_0]\{\psi_n\} = E_n[E]\{\psi_n\}. \quad (53)$$

Using these eigenstates, we can then expand  $\psi$  as

$$\{\psi(t)\} = \sum_{n=0}^{N_{\text{eig}}} c_n(t)\{\psi_n\}. \quad (54)$$

In many situations, it is common to only consider  $N_{\text{eig}} = 3$  for a transmon qubit [2]. However, as will be discussed in Section IV, this can lead to significantly incorrect results if one is not careful with the design of the incident pulses on the transmission line. This has also been noted as a deficiency in the quantum control literature for transmon qubits [46].

Now, the orthonormality of the transmon eigenstates then greatly simplifies the discretization of the time-dependent Schrödinger equation (41). In particular, we have

$$i\hbar \frac{d}{dt}\{c\} = [\mathcal{E}]\{c\} - i2e\beta(\partial_t\phi(z_0, t))[Q]\{c\}, \quad (55)$$

where  $\{c\} = [c_0, c_1, \dots, c_{N_{\text{eig}}}]^T$ . We further have that

$$[\mathcal{E}]_{mn} = \delta_{mn}E_n, \quad (56)$$

$$[Q]_{mn} = \{\psi_m\}^\dagger [Q]\{\psi_n\}, \quad (57)$$

where  $\delta_{mn}$  is a Kronecker delta and a superscript  $\dagger$  denotes a conjugate transpose. Following the same temporal discretization strategy of Section III-A, the time stepping equation for (55) is

$$\{c^{(j+3/2)}\} = \{c^{(j-1/2)}\} + \frac{2\Delta t}{i\hbar}[\mathcal{E}]\{c^{(j+1/2)}\} - \frac{4e\beta\Delta t}{\hbar}(\partial_t\phi^{(j+1/2)}(z_0))[Q]\{c^{(j+1/2)}\}. \quad (58)$$

This equation can be solved along with (49) to march the overall system of equations forward in time.

### C. Stability Analysis

As with any time domain method, a stability analysis is necessary to determine what values of  $\Delta t$  the system of equations can be safely solved for. The discretization strategies used in Sections III-A and III-B lead to conditionally stable systems, for which stability conditions can be derived using standard methods.

To begin, we will consider the wave equation for the nodal flux, whose time stepping equation was given in (49). This time stepping equation exactly matches the format of a typical full-wave FETD system, and so the same stability condition holds [45], [47]. From a Z-transform analysis, the stability condition is found to be

$$\Delta t \leq \frac{2}{\sqrt{\rho([T]^{-1}[S])}}, \quad (59)$$

where  $\rho([A])$  denotes the spectral radius of  $[A]$ .

The analysis of the stability condition for (51) and (58) can be found following the basic procedure of [48]. In this approach, a constraint on the temporal eigenvalues of the time-dependent Schrödinger equation are found. The temporal eigenvalues are given by

$$i\hbar\partial_t\psi = \lambda\psi, \quad (60)$$

where we use a generic notation of  $\psi$  since the approach works the same for (51) and (58). After applying the central difference formula, we have

$$i\hbar \frac{\psi^{(j+1)} - \psi^{(j-1)}}{2\Delta t} = \lambda\psi^{(n)}. \quad (61)$$

An amplification factor can be defined as  $g = \psi^{(n+1)}/\psi^{(n)} = \psi^{(n)}/\psi^{(n-1)}$ , where stability will only occur if  $|g| \leq 1$ . The amplification factor can be substituted into (61) and  $g$  can be solved for as

$$g = -i \frac{\lambda\Delta t}{\hbar} \pm \sqrt{1 - \left(\frac{\lambda\Delta t}{\hbar}\right)^2}. \quad (62)$$

For  $|g| \leq 1$ , we find that our stability condition is

$$\Delta t \leq \frac{\hbar}{\lambda}. \quad (63)$$

Now, the manner of computing  $\lambda$  depends on whether (51) or (58) is being solved. For (51), the  $\lambda$  is related to the eigenvalues of the matrix system on the right-hand side of (43) after multiplying by  $[E]^{-1}$ . Since this matrix system changes

depending on the value of  $\partial_t \phi(z_0, t)$ , it is not possible to find a “true” stability condition that is always valid. Instead, we make an estimate for the stability condition by using the maximum value expected for  $\partial_t \phi(z_0, t)$  to occur in a given simulation, which can be inferred reasonably well from the temporal profile of the voltage source that excites the transmission line. If we denote this maximum value of  $\partial_t \phi(z_0, t)$  as  $V_{\max}(z_0)$ , then we can estimate the stability condition as

$$\Delta t \leq \frac{\hbar}{\rho \left( [E]^{-1} ([H_0] - i2e\beta V_{\max}(z_0)[Q]) \right)} \quad (64)$$

Similarly, the stability condition for (58) is related to the eigenvalues of the matrix system on the right-hand side of (55). We can estimate the stability condition for (58) as

$$\Delta t \leq \frac{\hbar}{\rho \left( [\mathcal{E}] - i2e\beta V_{\max}(z_0)[Q] \right)}. \quad (65)$$

We have verified these stability conditions with numerical experiments, but do not show details of this for brevity.

Although the forms of the stability conditions (64) and (65) are very similar, in practice they produce very different numerical values. Generally, we find that (65) leads to a stability condition that is around  $O(10^3)$  larger than that of (64). Given that (64) is also often  $O(10^2)$  smaller than (59), this represents a significant advantage of using the reduced eigenstate expansion approach for forming the Maxwell-Schrödinger system of equations.

#### IV. NUMERICAL RESULTS

We present a range of numerical results in this section to validate the accuracy of the proposed formulation. We also investigate certain scenarios where our Maxwell-Schrödinger method can produce results that significantly differ from an approach that does not consider the self-consistent interaction between the transmon qubit and transmission line. We expect these scenarios will become increasingly important to explore as the design space is broadened to continue improving the performance of quantum devices that utilize transmon qubits.

We focus our numerical experiments on a simple device topology illustrated in Fig. 2. The device parameters are loosely based on a symmetrized version of the single photon source discussed in [9]. The simplicity of this device aids in determining parameter regimes where our numerical method should match established theoretical predictions, which we use to aid in validating our method. In all simulations, we use a practical ratio of  $E_J/E_C = 25$ . We always maintain  $C_\Sigma = C_g + C_q = 55$  fF to ensure that the transition frequencies of the transmon qubit remain the same regardless of the coupling strength  $\beta$  that we use in a particular simulation. For reference, the first transition frequency of the transmon is 4.60 GHz and the second transition frequency is 4.14 GHz. For transmission line parameters, we have that the per-unit-length parameters are  $L = 0.7125 \mu\text{H}/\text{m}$  and  $C = 285 \text{ pF}/\text{m}$ .

The remainder of this section is organized in the following manner. In Section IV-A, we consider the use of classical microwave signals to control the state of the transmon qubit. Following this, we discuss in Section IV-B the use of classical

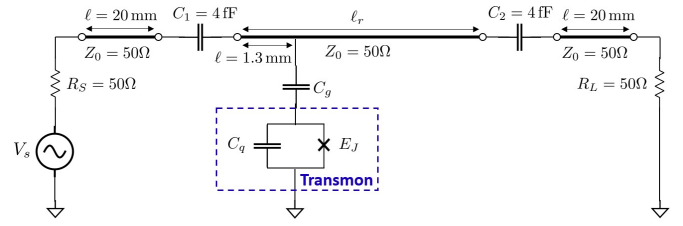


Fig. 2: Circuit schematic of the system analyzed in this work. Bold lines denote transmission lines, while thin lines denote a regular circuit connection. Parameters that do not have quantities explicitly given are varied for the different numerical experiments and are discussed in the main text.

microwave signals to measure the state of the transmon qubit using a dispersive readout procedure [2], [34], [35]. In each section, we review the basic details of the theoretical predictions that we use in validating our numerical method prior to discussing the numerical results.

#### A. Qubit Control

One of the most common and simple microwave control methods for modifying the state of a transmon qubit is to drive the qubit via a modulated Gaussian pulse with a center frequency near the first transition frequency of the qubit [2]. In the ideal case, this leads to a form of “driven” Rabi oscillation where the qubit state at the end of the microwave pulse varies in a cyclic manner between the ground and first excited state depending on the “pulse area” of the baseband Gaussian pulse [49]. By controlling the relative phase of the applied microwave pulses (e.g., via IQ modulation), sufficiently arbitrary output superposition states of the transmon qubit can be achieved to cover the needs of practical applications [2].

However, due to the weak nonlinearity of transmon qubits, the first and second transition frequencies are not significantly different. As a result, simple theoretical treatments of analyzing driven Rabi oscillations often will not yield exact results. For simple topologies, this can typically be accounted for by using narrowband pulses that reduce the unintentional effects combined with performing suitable calibration of pulse areas experimentally. Other more sophisticated pulses can also be used to minimize these issues [2], [50].

Here, we calibrate a  $2\pi$ -pulse that transitions the qubit from the ground state to the first excited state and then back to the ground state using numerical experiments, and then use this result to extrapolate to other pulse areas. For this set of simulations, we use a Gaussian pulse with a standard deviation of  $\sigma = 5$  ns,  $l_r = 8.77$  mm, and  $\beta = 0.01$ . This value of  $\beta$  is rather small for the circuit topology of Fig. 2, but keeps the interaction between the two subsystems small enough that we can initially validate our results against a simpler treatment that does not consider the interaction self-consistently. In particular, the simpler approach corresponds to neglecting the effect of the semiclassical current source in (26) to only allow one-way coupling of the signals in the transmission line onto the transmon.



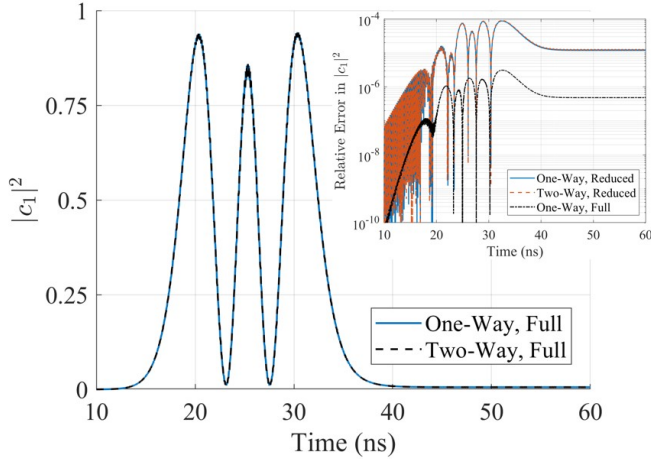


Fig. 3: Probability of finding the transmon in the first excited state as a function of time for a  $6\pi$ -pulse when  $\beta = 0.01$  and  $\sigma = 5$  ns. Cases considered include when there is a self-consistent semiclassical current source (two-way) or there is not one (one-way), and whether a full FETD discretization (full) or a reduced eigenstate discretization (reduced) is used. The inset shows that the relative error is very small for all methods, where the self-consistent method that uses a full FETD discretization is considered the reference.

To show our methods match expected theoretical results, we present the numerical results of the various methods discussed in this work for a  $6\pi$ -pulse in Fig. 3. This pulse area should complete three full Rabi oscillation cycles and end with the qubit state back in the ground state. We see that all of the numerical results demonstrate this behavior and maintain close agreement throughout the entire course of the simulation. For the simulations using the reduced eigenstate discretization of Section III-B, only the first three eigenstates of the transmon were included in the simulation. This is generally considered to be the minimum number of eigenstates needed to describe the dynamics of the transmon, and we see that in this simple scenario this is indeed adequate. Higher convergence can be achieved by including more eigenstates in the simulation.

Next, we look at less trivial scenarios where the capability of a numerical method is of more value. In particular, we increase  $\beta$  to 0.1, which is a more realistic value for a resonator coupled to a transmon qubit in modern designs (see, e.g., [16]). We also keep the Gaussian pulse  $\sigma = 5$  ns, but adjust the pulse amplitude to correspond to a  $5.5\pi$ -pulse that should transition the transmon into an equal superposition of its first two states after 2.5 Rabi oscillation cycles. From the results in Fig. 4, we see that there begins to be a discrepancy in the final state between the self-consistent method and the approach that only allows one-way coupling. This deviation is easily understood to occur due to the back-action of the transmon qubit on the transmission line, and is, in principle, easily correctable through experimental calibration. It should also be noted, that for this example four eigenstates of the transmon are necessary to achieve good convergence in the dynamics between the various methods. The increased number of eigenstates is also due to the increased coupling between the two subsystems.

Now, if we attempt to shorten the duration of the Gaussian pulse to  $\sigma = 1.5$  ns while increasing the pulse amplitude to

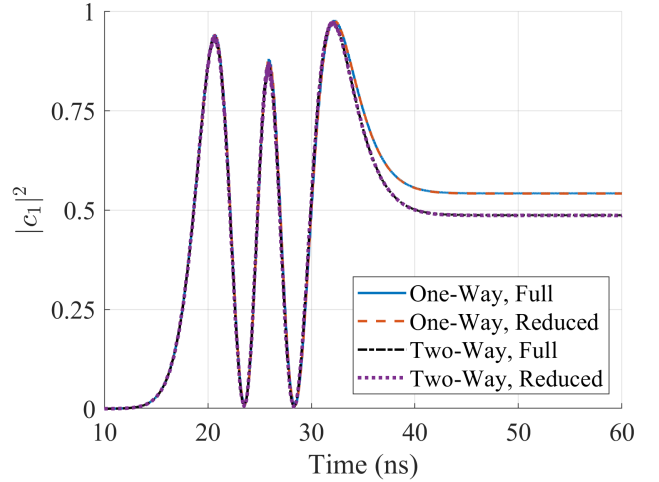


Fig. 4: Probability of finding the transmon in the first excited state as a function of time for a  $5.5\pi$ -pulse when  $\beta = 0.1$  and  $\sigma = 5$  ns. The increased coupling between the systems results in the deviation between the approaches considering a self-consistent semiclassical current source (two-way) and the approaches that neglect this interaction (one-way). Excellent convergence is still achieved between the full FETD (full) and reduced eigenstate (reduced) discretizations.

still achieve a  $5.5\pi$ -pulse, we see in Fig. 5 that non-trivial dynamical effects begin to emerge. From a simplified theoretical treatment, the final state of the transmon qubit should be identical between Figs. 4 and 5. The deviation is due to non-negligible interactions with higher transmon eigenstates, which are neglected in the theoretical treatment. We further see that there are now significant deviations between the results of our self-consistent method and the method that only considers one-way coupling in Fig. 5. This is due purely to the back action of the transmon on the transmission line. The periodicity in these additional dynamics suggests that this effect is due to wave interference effects within the transmission line resonator. In order to achieve convergence in these dynamics, six eigenstates of the transmon were needed.

The need for this many eigenstates in quantum control analysis is not unprecedented, with the results of [46] suggesting that as many as 13 eigenstates can be needed to achieve convergence in transmon dynamics for realistic pulse designs. An exhaustive study on the number of eigenstates needed for convergence is outside of the scope of this work, but for the modeling of a single qubit the computational cost of including additional eigenstates in the numerical method is negligible. However, as these methods are adapted to considering multi-qubit interactions in the future, a more detailed understanding of the needed number of eigenstates will become essential to minimize the size of the overall Hilbert space that the dynamics need to be modeled within.

### B. Qubit State Measurement

The state of the transmon qubit can be measured via microwave transmission or reflection measurements of the transmission line resonator [2]. Known as dispersive readout, this approach utilizes the transmon state-dependent “dispersive shift” that is applied to the transmission line resonant



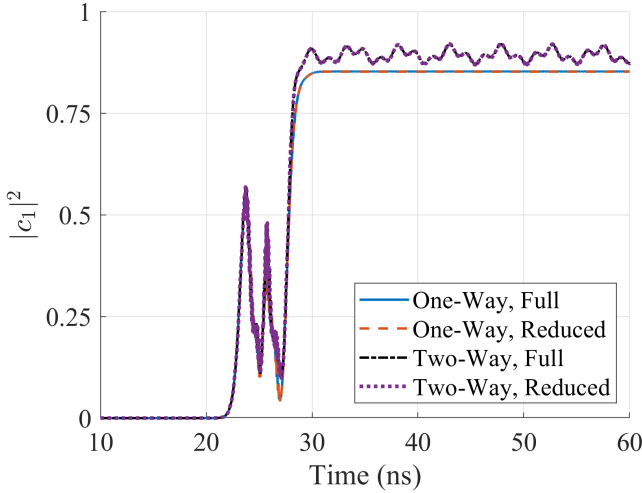


Fig. 5: Probability of finding the transmon in the first excited state as a function of time for a  $5.5\pi$ -pulse when  $\beta = 0.1$  and  $\sigma = 1.5$  ns. The shorter pulsewidth results in non-negligible interactions with higher transmon eigenstates and the transmission line, which causes significant discrepancy between approaches considering a self-consistent semiclassical current source (two-way) and the approaches that neglect this interaction (one-way). Excellent convergence is still achieved between the full FETD (full) and reduced eigenstate (reduced) discretizations.

frequency due to the interaction between the transmission line and transmon. This effect is commonly derived using methods of cavity quantum electrodynamics, which utilizes a quantum treatment of the electromagnetic field [1], [34]. Here, we show that our semiclassical modeling approach can replicate the correct dispersive shift of the transmission line resonator without requiring any quantum treatment of the resonator.

To begin, we briefly review certain details of the cavity quantum electrodynamics treatment that are needed to substantiate the numerical results presented later. To facilitate this, we briefly adopt the Dirac bra-ket notation that is helpful for expressing the generalized Jaynes-Cummings Hamiltonian that is applicable to the transmon and transmission line resonator system. In particular, we denote the  $m$ th eigenstate of the free transmon Hamiltonian (14) as  $|m\rangle$  and the conjugate transpose of this state as  $\langle m|$ . The generalized Jaynes-Cummings Hamiltonian is then

$$\hat{H} = \sum_m \hbar\omega_m |m\rangle\langle m| + \hbar\omega_r \hat{a}^\dagger \hat{a} + \left( \sum_m \hbar g_{m,m+1} |m\rangle\langle m+1| \hat{a}^\dagger + \text{H.c.} \right), \quad (66)$$

where  $\omega_m$  is the angular resonant frequency of the  $m$ th transmon state,  $\omega_r$  is the angular resonant frequency of the transmission line, and  $\hat{a}$  and  $\hat{a}^\dagger$  are the annihilation and creation operators of the transmission line resonator, respectively [34]. The coupling strength between the transmon and transmission line is set by  $g_{m,m+1}$ , which is given by [34]

$$\hbar g_{m,m+1} = 2e\beta \sqrt{\frac{\hbar\omega_r}{2\ell_r C}} \langle m|\hat{n}|m+1\rangle = \hbar g_{m+1,m}^*. \quad (67)$$

The dispersive limit of cavity quantum electrodynamics is

typically considered to be a valid approximation when the coupling strength is small relative to the detuning between the transmon and transmission line resonant frequencies. More explicitly, it requires

$$\frac{g_{0,1}}{|\omega_{0,1} - \omega_r|} \ll 1, \quad (68)$$

where  $\omega_{m,n} = \omega_m - \omega_n$  is a shorthand for the transmon transition frequency between two states  $|m\rangle$  and  $|n\rangle$ . For a transmon that is weakly nonlinear, this condition is sometimes also extended to additionally require [34]

$$\frac{g_{0,1}}{|\omega_{1,2} - \omega_r|} \ll 1. \quad (69)$$

In the dispersive limit, it is possible to transform the generalized Jaynes-Cummings Hamiltonian (66) into a simplified form that eliminates the direct interaction terms up to second order in the small parameter  $g_{0,1}/|\omega_{0,1} - \omega_r|$ . By only keeping the two lowest levels of the transmon qubit after performing the necessary transformation, the resulting approximate Hamiltonian becomes

$$\hat{H} \approx \frac{\hbar\omega'_{0,1}}{2} (|1\rangle\langle 1| - |0\rangle\langle 0|) + \hbar(\omega'_r + \chi|1\rangle\langle 1| - \chi|0\rangle\langle 0|) \hat{a}^\dagger \hat{a}, \quad (70)$$

where  $\omega'_{0,1} = \omega_{0,1} + \chi_{0,1}$  and  $\omega'_r = \omega_r - \chi_{1,2}/2$  [34]. The state-independent partial dispersive shifts are given by

$$\chi_{m,n} = \frac{g_{m,n}^2}{\omega_{m,n} - \omega_r}, \quad (71)$$

and the state-dependent dispersive shift is given by

$$\chi = \chi_{0,1} - \chi_{1,2}/2. \quad (72)$$

The measurement of the qubit state is accomplished by recognizing that if the measurement collapses the transmon into the  $|0\rangle$  state then the effective resonant frequency of the transmission line resonator will be  $\omega'_r - \chi$ , while if the measurement collapses the transmon into the  $|1\rangle$  state then the resonant frequency will be  $\omega'_r + \chi$ .

As a first numerical example, we consider the case of the transmon and resonator detuning  $\omega_{0,1} - \omega_r$  being negative. For this case, the resonator length is  $\ell_r = 6.498$  mm and the coupling strength is set by  $\beta = 0.25$ . This value of  $\beta$  is closer to that of the device the circuit topology of Fig. 2 is based on, and is selected to provide a significant dispersive shift that makes the shifted resonant peaks of the transmission through the resonator clearly distinguishable. Given the above parameters, we compute the various dispersive shifts and find that  $\chi_{0,1}/2\pi = -14.620$  MHz,  $\chi_{1,2}/2\pi = -17.137$  MHz, and  $\chi/2\pi = -6.052$  MHz.

To check our numerical method against these analytical results, we perform three simulations. The first considers the case with no transmon present to determine the bare resonant frequency of the transmission line resonator. The next two simulations include the transmon, but as initial conditions start the transmon in the  $|0\rangle$  or  $|1\rangle$  state. The  $|S_{21}|$  of the transmission line circuit is extracted for all of these simulations and is shown in Fig. 6. The locations of the resonant peaks are

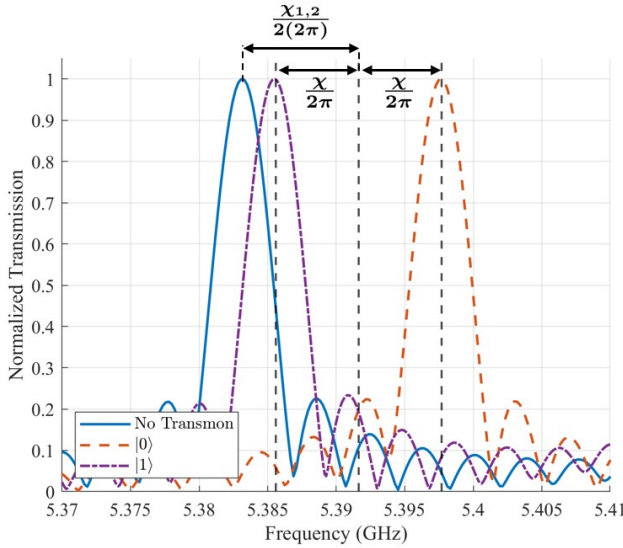


Fig. 6: Simulation results of dispersive readout for the negative detuning case. Vertical dashed lines mark the relevant frequencies computed using the theoretically derived  $\chi_{0,1}$ ,  $\chi_{1,2}$ , and  $\chi$ .

compared against the theoretical predictions in Fig. 6, where it is seen that the agreement between the theoretical result and our numerical method is excellent.

Note that due to the high  $Q$  of the transmission line resonator, these simulations require a longer total time than the qubit control simulations considered in Section IV-A. To more easily accommodate this, we used the reduced eigenstate discretization with 15 eigenstates to produce these results to avoid the significantly smaller  $\Delta t$  needed when using a full FETD discretization. We verified our simulation results against a full FETD simulation for the transmon starting in the  $|0\rangle$  state, and found good agreement. Hence, we proceed in this section with only considering reduced eigenstate discretizations.

Next, we consider the case of positive detuning where  $\omega_{0,1} - \omega_r > 0$ . This setup can have attractive operating characteristics for different qubit control and measurement protocols [34]. However, it can be more difficult to operate in the positive detuning regime because the transitions to higher transmon states generally occur at lower frequencies than  $\omega_{0,1}$ , which can end up stressing the approximations of the dispersive regime in (69).

To illustrate this, we set the resonator length to  $\ell_r = 8.77$  mm and the coupling strength to  $\beta = 0.25$ . Given these parameters, the dispersive shifts are  $\chi_{0,1}/2\pi = 10.308$  MHz,  $\chi_{1,2}/2\pi = 74.368$  MHz, and  $\chi/2\pi = -26.876$  MHz. Additionally, for the above settings, the right-hand side of (69) is  $\sim 0.52$ , which violates part of the dispersive regime approximation. However, as shown in Fig. 7, the effects of the dispersive shift are still clearly seen in the numerical results. Despite this, it is found that the theoretical results are no longer in strong agreement with the numerical results due to the violation of the approximations made in the theoretical analysis. It is interesting to note that the difference in resonant frequencies is still  $\sim 2\chi$ , but the center point that these resonant frequencies are displaced from is shifted by  $\sim 3$  MHz compared

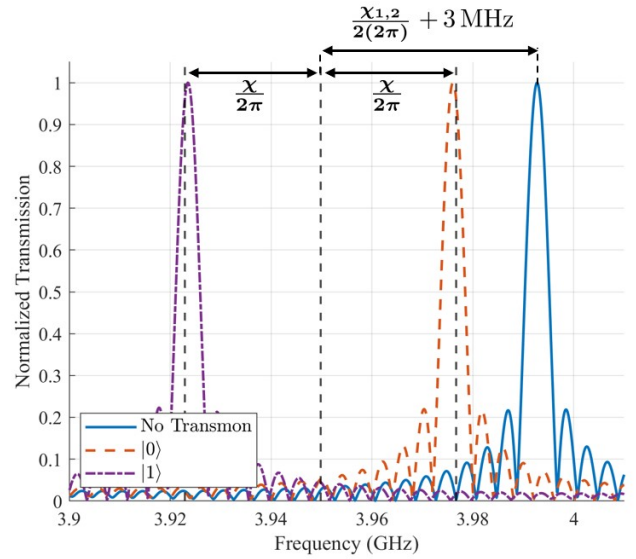


Fig. 7: Simulation results of dispersive readout for the positive detuning case. Vertical dashed lines mark the relevant frequencies computed using the theoretically derived  $\chi_{0,1}$ ,  $\chi_{1,2}$ , and  $\chi$ . These lines are all shifted by an additional 3 MHz to align them with the numerical results. This correction is needed due to approximations in the theoretical analysis being violated, as discussed in the main text.

to the theoretical result.

These results highlight that this numerical method can successfully predict important aspects of dispersive readout protocols for measuring the state of transmon qubits. Our numerical method does not require restrictive assumptions on operating regimes for theoretical predictions to be made, allowing for a wider design space to be explored rapidly. This can potentially be utilized in the future to design faster and higher fidelity readout protocols, as well as to push the boundaries on what parameters are considered viable in the design stages of new devices.

## V. CONCLUSION

In this work, we presented the formulation of a self-consistent one-dimensional Maxwell-Schrödinger method for analyzing the interactions between a transmon qubit and classical microwave signals on transmission lines. We discussed two different discretization strategies that can be used to solve the Maxwell-Schrödinger system of equations for general transmission line geometries. We presented numerical examples that demonstrated that our hybrid numerical method produces results consistent with theoretical predictions in operating regimes where the theoretical predictions are valid. We also showed that our numerical method can still produce reasonable results in operating regimes where theoretical predictions become invalid, providing a new tool for rapidly exploring a larger design space in the future for optimizing the control and measurement of the state of transmon qubits.

Future work can consider extending this class of Maxwell-Schrödinger methods in a number of ways. For instance, although transmon qubits are heavily-favored experimentally, there exist many other cQED qubits that could be analyzed in

a similar way [1], [2]. Although a one-dimensional model is advantageous for its efficiency, emerging device architectures will require the higher accuracy that full-wave methods provide, and so it is also of interest to develop full-wave Maxwell-Schrödinger methods for cQED systems. Finally, incorporating multi-qubit interactions is of significant interest to be able to model multi-qubit gates that are necessary to produce entanglement in quantum devices. Similarly, there are many deleterious multi-qubit interactions in the form of classical and quantum crosstalk that Maxwell-Schrödinger methods can potentially model. Gaining more insight into these effects in practical devices is of significant interest to improve the performance of emerging cQED devices, and represents an important avenue for future numerical modeling work.

## REFERENCES

- [1] X. Gu, A. F. Kockum, A. Miranowicz, Y.-X. Liu, and F. Nori, “Microwave photonics with superconducting quantum circuits,” *Physics Reports*, vol. 718, pp. 1–102, 2017.
- [2] P. Krantz, M. Kjaergaard, F. Yan, T. P. Orlando, S. Gustavsson, and W. D. Oliver, “A quantum engineer’s guide to superconducting qubits,” *Applied Physics Reviews*, vol. 6, no. 2, p. 021318, 2019.
- [3] A. Blais, A. L. Grimsmo, S. M. Girvin, and A. Wallraff, “Circuit quantum electrodynamics,” *Reviews of Modern Physics*, vol. 93, no. 2, p. 025005, 2021.
- [4] R. Ma, B. Saxberg, C. Owens, N. Leung, Y. Lu, J. Simon, and D. I. Schuster, “A dissipatively stabilized Mott insulator of photons,” *Nature*, vol. 566, no. 7742, pp. 51–57, 2019.
- [5] L. Lamata, A. Parra-Rodriguez, M. Sanz, and E. Solano, “Digital-analog quantum simulations with superconducting circuits,” *Advances in Physics: X*, vol. 3, no. 1, p. 1457981, 2018.
- [6] F. Arute, K. Arya, R. Babbush, D. Bacon, J. C. Bardin, R. Barends, R. Biswas, S. Boixo, F. G. Brandao, D. A. Buell *et al.*, “Quantum supremacy using a programmable superconducting processor,” *Nature*, vol. 574, no. 7779, pp. 505–510, 2019.
- [7] Y. Wu, W.-S. Bao, S. Cao, F. Chen, M.-C. Chen, X. Chen, T.-H. Chung, H. Deng, Y. Du, D. Fan *et al.*, “Strong quantum computational advantage using a superconducting quantum processor,” *Physical Review Letters*, vol. 127, no. 18, p. 180501, 2021.
- [8] P. Jurcevic, A. Javadi-Abhari, L. S. Bishop, I. Lauer, D. F. Bogorin, M. Brink, L. Capelluto, O. Günlük, T. Itoko, N. Kanazawa *et al.*, “Demonstration of quantum volume 64 on a superconducting quantum computing system,” *Quantum Science and Technology*, vol. 6, no. 2, p. 025020, 2021.
- [9] A. A. Houck, D. Schuster, J. Gambetta, J. Schreier, B. Johnson, J. Chow, L. Frunzio, J. Majer, M. Devoret, S. Girvin *et al.*, “Generating single microwave photons in a circuit,” *Nature*, vol. 449, no. 7160, pp. 328–331, 2007.
- [10] Y. Zhou, Z. Peng, Y. Horiuchi, O. Astafiev, and J. Tsai, “Tunable microwave single-photon source based on transmon qubit with high efficiency,” *Physical Review Applied*, vol. 13, no. 3, p. 034007, 2020.
- [11] C. Lang, C. Eichler, L. Steffen, J. Fink, M. J. Woolley, A. Blais, and A. Wallraff, “Correlations, indistinguishability and entanglement in Hong–Ou–Mandel experiments at microwave frequencies,” *Nature Physics*, vol. 9, no. 6, pp. 345–348, 2013.
- [12] M. Reagor, W. Pfaff, C. Axline, R. W. Heeres, N. Ofek, K. Sliwa, E. Holland, C. Wang, J. Blumoff, K. Chou *et al.*, “Quantum memory with millisecond coherence in circuit QED,” *Physical Review B*, vol. 94, no. 1, p. 014506, 2016.
- [13] K. Sardashti, M. C. Dartailh, J. Yuan, S. Hart, P. Gumann, and J. Shabani, “Voltage-tunable superconducting resonators: a platform for random access quantum memory,” *IEEE Transactions on Quantum Engineering*, vol. 1, pp. 1–7, 2020.
- [14] N. Leung, Y. Lu, S. Chakram, R. K. Naik, N. Earnest, R. Ma, K. Jacobs, A. N. Cleland, and D. I. Schuster, “Deterministic bidirectional communication and remote entanglement generation between superconducting qubits,” *npj Quantum Information*, vol. 5, no. 1, pp. 1–5, 2019.
- [15] Z. Chen, K. J. Satzinger, J. Atalaya, A. N. Korotkov, A. Dunsworth, D. Sank, C. Quintana, M. McEwen, R. Barends, P. V. Klimov *et al.*, “Exponential suppression of bit or phase errors with cyclic error correction,” *Nature*, vol. 595, no. 7867, pp. 383–387, 2021.
- [16] S. Kosen, H.-X. Li, M. Rommel, D. Shiri, C. Warren, L. Grönberg, J. Salonen, T. Abad, J. Biznárová, M. Caputo *et al.*, “Building blocks of a flip-chip integrated superconducting quantum processor,” *Quantum Science and Technology*, vol. 7, no. 3, p. 035018, 2022.
- [17] C. Conner, A. Bienfait, H.-S. Chang, M.-H. Chou, É. Dumur, J. Grebel, G. Peairs, R. Povey, H. Yan, Y. Zhong *et al.*, “Superconducting qubits in a flip-chip architecture,” *Applied Physics Letters*, vol. 118, no. 23, p. 232602, 2021.
- [18] D. Rosenberg, D. Kim, R. Das, D. Yost, S. Gustavsson, D. Hover, P. Krantz, A. Melville, L. Racz, G. Samach *et al.*, “3D integrated superconducting qubits,” *npj Quantum Information*, vol. 3, no. 1, pp. 1–5, 2017.
- [19] Y. Xu, G. Huang, J. Balewski, R. Naik, A. Morvan, B. Mitchell, K. Nowrouzi, D. I. Santiago, and I. Siddiqi, “QubiC: An open-source FPGA-based control and measurement system for superconducting quantum information processors,” *IEEE Transactions on Quantum Engineering*, vol. 2, pp. 1–11, 2021.
- [20] J. C. Bardin, E. Jeffrey, E. Lucero, T. Huang, O. Naaman, R. Barends, T. White, M. Giustina, D. Sank, P. Roushan *et al.*, “A 28nm bulk-CMOS 4-to-8 GHz 2 mW cryogenic pulse modulator for scalable quantum computing,” in *2019 IEEE International Solid-State Circuits Conference-(ISSCC)*. IEEE, 2019, pp. 456–458.
- [21] B. Patra, J. P. van Dijk, S. Subramanian, A. Corna, X. Xue, C. Jeon, F. Sheikh, E. Juarez-Hernandez, B. P. Esparza, H. Rampurwala *et al.*, “A scalable cryo-CMOS 2-to-20 GHz digitally intensive controller for 4×32 frequency multiplexed spin qubits/transmons in 22nm FinFET technology for quantum computers,” in *2020 IEEE International Solid-State Circuits Conference-(ISSCC)*. IEEE, 2020, pp. 304–306.
- [22] F. Solgun, D. P. DiVincenzo, and J. M. Gambetta, “Simple impedance response formulas for the dispersive interaction rates in the effective Hamiltonians of low anharmonicity superconducting qubits,” *IEEE Transactions on Microwave Theory and Techniques*, vol. 67, no. 3, pp. 928–948, 2019.
- [23] T. E. Roth and W. C. Chew, “Macroscopic circuit quantum electrodynamics: A new look toward developing full-wave numerical models,” *IEEE Journal on Multiscale and Multiphysics Computational Techniques*, vol. 6, pp. 109–124, 2021.
- [24] Z. K. Mineev, Z. Leghtas, S. O. Mundhada, L. Christakis, I. M. Pop, and M. H. Devoret, “Energy-participation quantization of Josephson circuits,” *npj Quantum Information*, vol. 7, no. 1, pp. 1–11, 2021.
- [25] T. E. Roth and W. C. Chew, “Full-wave modeling of the emission of a microwave frequency single photon source,” in *2021 International Applied Computational Electromagnetics Society Symposium (ACES)*. IEEE, 2021, pp. 1–4.
- [26] ———, “Full-wave methodology to compute the spontaneous emission rate of a transmon qubit,” *IEEE Journal on Multiscale and Multiphysics Computational Techniques*, vol. 7, pp. 92–101, 2022.
- [27] M. Sindelka, “Derivation of coupled Maxwell-Schrödinger equations describing matter-laser interaction from first principles of quantum electrodynamics,” *Physical Review A*, vol. 81, no. 3, p. 033833, 2010.
- [28] M. O. Scully and M. S. Zubairy, *Quantum Optics*. Cambridge University Press, 2001.
- [29] T. Takeuchi, S. Ohnuki, and T. Sako, “Maxwell-Schrödinger hybrid simulation for optically controlling quantum states: A scheme for designing control pulses,” *Physical Review A*, vol. 91, no. 3, p. 033401, 2015.
- [30] C. J. Ryu, A. Y. Liu, W. E. I. Sha, and W. C. Chew, “Finite-difference time-domain simulation of the Maxwell-Schrödinger system,” *IEEE Journal on Multiscale and Multiphysics Computational Techniques*, vol. 1, pp. 40–47, 2016.
- [31] C. Xiang, F. Kong, K. Li, and M. Liu, “A high-order symplectic FDTD scheme for the Maxwell-Schrodinger system,” *IEEE Journal of Quantum Electronics*, vol. 54, no. 1, pp. 1–8, 2017.
- [32] Y. P. Chen, W. E. I. Sha, L. Jiang, M. Meng, Y. M. Wu, and W. C. Chew, “A unified Hamiltonian solution to Maxwell-Schrödinger equations for modeling electromagnetic field-particle interaction,” *Computer Physics Communications*, vol. 215, pp. 63–70, 2017.
- [33] C. Xiang, F. Kong, K. Li, and M. Liu, “A quantum state controller based on the electromagnetic potentials,” *IEEE Access*, vol. 7, pp. 42006–42013, 2019.
- [34] J. Koch, M. Y. Terri, J. Gambetta, A. A. Houck, D. Schuster, J. Majer, A. Blais, M. H. Devoret, S. M. Girvin, and R. J. Schoelkopf, “Charge-insensitive qubit design derived from the Cooper pair box,” *Physical Review A*, vol. 76, no. 4, p. 042319, 2007.
- [35] T. E. Roth, R. Ma, and W. C. Chew, “The transmon qubit for electromagnetics engineers: An introduction,” *IEEE Antennas and Propagation Magazine*, 2022.

- [36] W. C. Chew, D. Y. Na, P. Bermel, T. E. Roth, C. J. Ryu, and E. Kudeki, "Quantum Maxwell's equations made simple: Employing scalar and vector potential formulation," *IEEE Antennas and Propagation Magazine*, vol. 63, no. 1, pp. 14–26, 2021.
- [37] W. C. Chew, A. Y. Liu, C. Salazar-Lazaro, and W. E. I. Sha, "Quantum electromagnetics: A new look—Part I," *IEEE Journal on Multiscale and Multiphysics Computational Techniques*, vol. 1, pp. 73–84, 2016.
- [38] —, "Quantum electromagnetics: A new look—Part II," *IEEE Journal on Multiscale and Multiphysics Computational Techniques*, vol. 1, pp. 85–97, 2016.
- [39] S. M. Girvin, "Circuit QED: Superconducting qubits coupled to microwave photons," in *Quantum Machines: Measurement and Control of Engineered Quantum Systems*. Oxford University Press, 2014, pp. 113–256.
- [40] M. O. Hecht, A. J. Cobarrubia, and K. M. Sundqvist, "An engineer's brief introduction to microwave quantum optics and a single-port state-space representation," *IEEE Transactions on Quantum Engineering*, vol. 2, pp. 1–8, 2021.
- [41] D. M. Pozar, *Microwave Engineering*. John Wiley & Sons, 2009.
- [42] M. Tinkham, *Introduction to Superconductivity*, 2nd ed. Dover Publications, 2004.
- [43] H. Haken, *Quantum Field Theory of Solids: An Introduction*. North-Holland Publishing Company, 1976.
- [44] C. Cohen-Tannoudji, J. Dupont-Roc, and G. Grynberg, *Photons and Atoms: Introduction to Quantum Electrodynamics*. Wiley Interscience, 1997.
- [45] J.-M. Jin, *The Finite Element Method in Electromagnetics*, 3rd ed. John Wiley & Sons, 2015.
- [46] T. Jones, K. Steven, X. Poncini, M. Rose, and A. Fedorov, "Approximations in transmon simulation," *Physical Review Applied*, vol. 16, no. 5, p. 054039, 2021.
- [47] D. Jiao and J.-M. Jin, "A general approach for the stability analysis of the time-domain finite-element method for electromagnetic simulations," *IEEE Transactions on Antennas and Propagation*, vol. 50, no. 11, pp. 1624–1632, 2002.
- [48] A. Soriano, E. A. Navarro, J. A. Porti, and V. Such, "Analysis of the finite difference time domain technique to solve the Schrödinger equation for quantum devices," *Journal of Applied Physics*, vol. 95, no. 12, pp. 8011–8018, 2004.
- [49] M. Fox, *Quantum Optics: An Introduction*. Oxford University Press, 2006, vol. 15.
- [50] F. Motzoi, J. M. Gambetta, P. Rebentrost, and F. K. Wilhelm, "Simple pulses for elimination of leakage in weakly nonlinear qubits," *Physical Review Letters*, vol. 103, no. 11, p. 110501, 2009.